In Search of Discernible Infrasound Emitted by Numerically Simulated Tornadoes

David A. Schecter*

NorthWest Research Associates, Redmond, WA 98052

Abstract

The comprehensive observational study of Bedard [2005] provisionally found that the infrasound of a tornado is discernible from the infrasound of generic cloud processes in a convective storm. This paper discusses an attempt to corroborate the reported observations of distinct tornado infrasound with numerical simulations. Specifically, this paper investigates the infrasound of an ordinary tornado in a numerical experiment with the Regional Atmospheric Modeling System, customized to simulate acoustic phenomena. The simulation has no explicit parameterization of microphysical cloud processes, but creates an unsteady tornado of moderate strength by constant thermal forcing in a rotational environment. Despite strong fluctuations in the lower corner flow and upper outflow regions, a surprisingly low level of infrasound is radiated by the vortex. Infrasonic pressure waves in the 0.1 Hz frequency regime are less intense than those which could be generated by core-scale vortex Rossby (VR) waves of modest amplitude in similar vortices. Higher frequency infrasound is at least an order of magnitude weaker than expected based on infrasonic observations of tornadic thunderstorms. Suppression of VR waves (and their infrasound) is explained by the gradual decay of axial vorticity with increasing radius from the center of the vortex core. Such non-Rankine wind-structure is known to enable the rapid damping of VR waves by inviscid mechanisms, including resonant wave-mean flow interaction and "spiral wind-up" of vorticity. Insignificant levels of higher frequency infrasound may be due to oversimplifications in the computational setup, such as the neglect of thermal fluctuations caused by phase transitions of moisture in vigorous cloud turbulence.

Keywords: tornadoes, infrasound, severe weather, numerical modeling, vortex Rossby waves

1. Introduction

1.1. Background and Objectives

Recent observational studies have shown that tornadic thunderstorms persistently emit acoustic radiation with an unusually strong component in the 0.5-10 Hz frequency range [Bedard 2005 (B05); Bedard et al. 2004; Szoke et al. 2004]. One might speculate that such infrasound is connected to repeated electrical discharges; however, Bedard reports no obvious correlation with lightning events [B05]. In theory, the infrasound could also come from condensation of water vapor, induced by mixing of temperature inhomogeneities in vigorous cloud turbulence [Akhalkatsi and Gogoberidze 2011]. The efficacy of this theoretical source mechanism does not require the presence of a coherent vortex in any obvious way. By contrast, Bedard presents a compelling case that the distinct 0.5-10 Hz infrasound of a tornadic thunderstorm originates from a tornado, or storm rotation conducive to tornadogenesis [B05]. If coherent vortices prove to be the prevailing source of the unusually strong signals, then monitoring infrasonic emissions could significantly improve tornado warning systems [ibid].

This paper will focus on the following fundamental question: how might the wind fluctuations of a generic tornado emit discernible infrasound? While the preceding question has been asked for decades [B05; Georges 1976; Georges and Greene 1975], the answer is not entirely clear.

Corresponding author address: David A. Schecter, Northwest Research Associates, 3380 Mitchell Lane, Boulder, CO 80301 (USA). *Phone:* 011-1-303-415-9701. *Fax:* 011-1-303-415-9702. *E-mail:* schecter@nwra.com.

Tornadoes are convective vortices that exhibit diverse fluctuations. Many (but not all) of these fluctuations emit acoustic radiation [Powell 1964; Howe 2003]. Schecter and collaborators examined the infrasound generated by vortex Rossby (VR) waves[1] in idealized tornadoes with purely Rankine structure [Schecter et al. 2008 (S08)]. Typical VR waves, and their acoustic radiation fields, have frequencies of order 0.1 Hz. This frequency regime falls below the 0.5 Hz cutoff of the aforementioned observational studies, and may be dominated by the infrasound of non-tornadic cloud processes [Bowman and Bedard 1971; Georges and Greene 1975; Akhalkatsi and Gogoberidze 2009]. Nevertheless, it is worthy of consideration on theoretical grounds. Numerical experiments in S08 provisionally showed that VR waves in a strong tornado can produce more powerful infrasound at ~0.1 Hz than a non-rotating cumulonimbus. It is possible that VR waves in more generic (non-Rankine) tornadoes are strongly damped, and unexcitable to significant amplitudes by natural forcing. One goal of the present study is to obtain further insight into the potential relevance of VR waves to the ~0.1 Hz infrasound of a tornadic thunderstorm.

Higher frequency emissions from a VR wave would require an azimuthal wavenumber n much greater than unity. Since the acoustic radiation field of a VR wave attenuates "exponentially" with increasing n, discernible emissions in the 0.5-10 Hz frequency range do not seem plausible under ordinary circumstances [S08]. Earlier studies had proposed that axisymmetric ($n = 0$) vibrations of the vortex core might account for the distinct 0.5-10 Hz emissions of a tornadic thunderstorm [Abdullah 1966; B05], but this hypothesis appears to have some fundamental deficiencies [Schecter 2012]. A second goal of the present study is to assess whether alternative modes of oscillation or more complicated wind fluctuations of a tornado might be responsible for the high frequency observations.

1.2. Basic Methodology

To address the issues posed above, this paper investigates the source and magnitude of the infrasound emitted by a generic tornado, simulated with a customized version of the Regional Atmospheric Modeling System (c-RAMS). The reader may consult Cotton et al. [2003] for a description of standard RAMS, and Medvigy et al. [2005] for a description of the pertinent customization [cf. Nicholls and Pielke 2000]. The model is fully compressible, allows multiple nested grids, and facilitates non-uniform vertical grid spacing. It has been shown that c-RAMS can adequately simulate classic mechanisms of vortex sound production [S08; Schecter 2011 (S11)]. It has also been shown that standard RAMS is capable of generating tornadoes through natural supercell convection under severe storm conditions [Grasso and Cotton 1995]. In principle, one could analyze the infrasound generated by tornadoes in similar supercell simulations carried out with c-RAMS. However, achieving adequate resolution would be prohibitively expensive. Moreover, acoustic peculiarities of standard cloud microphysics parameterizations could unnecessarily complicate the analysis, bearing in mind that the present goal is limited to understanding the infrasound produced solely by tornadic wind fluctuations [Schecter and Nicholls 2010; S11]. Simpler techniques with artificially driven convection have been developed for efficiently simulating quasi-realistic tornadoes at high resolution [e.g., Rotunno 1977; Fiedler 1998; Llewellen et al. 2000]. A variant that seems most akin to the Fiedler-technique is used here.

To review, the Fiedler simulations have no moisture, but impose artificial buoyancy forcing in the vertical momentum equation. The atmosphere starts at rest, but the Coriolis parameter is elevated to the vorticity that would exist in a mesocyclone. The artificial buoyancy forcing drives convection, which converges ambient angular momentum in the lower troposphere and generates a tornado.

The present simulations exclude moisture as well, but the buoyant updraft is created by explicit heating aloft. The Coriolis parameter is unchanged from its local planetary value, but a low-level cyclonic circulation provides elevated background vorticity to facilitate a process resembling non-supercell tornadogenesis [Wakimoto and Wilson 1989; Lee and Wilhelmson 1997]. The ambient atmosphere is stratified into a marginally stable boundary layer, a moderately stable free troposphere, and a strongly stable upper atmosphere. The surface layer applies quasi-realistic drag, and Rayleigh damping quenches upward propagating waves in the stratosphere. Radiation conditions are employed at the lateral boundaries to minimize the reflection of outward propagating acoustic waves.

[1] The term "vortex Rossby wave" belongs to the shared lexicon of dynamical meteorology and physical oceanography [Montgomery and Kallenbach 1997; McWilliams et al. 2003; Schecter and Montgomery 2003,2004]. It refers to a non-axisymmetric wave whose oscillation mechanism is connected to the radial gradient of axial vorticity (or potential vorticity). The classic example of a discrete VR wave is an azimuthally propagating elliptical deformation of the vortex core. Other VR waves propagate both azimuthally and radially, and are sheared by differential rotation.

1.3. Outline

The remainder of this paper is organized as follows. Section 2 elaborates upon the computational setup of the tornado simulations. Section 3 describes the basic structure of a simulated tornado. Section 4 describes the nature of the simulated infrasound. Section 5 assesses the significance of tornadic wind fluctuations to the production of infrasound in a severe storm, based on the present simulation results. Section 5 also provides evidence that VR waves are less relevant than previously thought. Section 6 explains the apparent suppression of VR waves in the vortex core. Section 7 offers some concluding remarks. Appendix A discusses a variety of acoustic sources that are possible in a c-RAMS simulation. Appendix B discusses a numerical subtlety pertaining to the artificial generation of high frequency infrasound at nested grid boundaries.

2. Computational Setup

The primary simulation of our study is called the "α-experiment." The α-experiment has four concentrically nested square grids, with horizontal increments of Δ_x = 3.6, 10.7, 32 and 128 m. The horizontal grid lengths are L = 1.2, 2.4, 6.5 and 26 km, respectively. The vertical mesh is the same for all grids, and is continuously stretched with height z over 300 grid points. The vertical grid spacing Δ_z is 4 m near the ground, 50 m at z = 3 km, and 170 m at z = 10 km. The model top is at z = 29 km.

The surface value of the ambient potential temperature $\theta_a(z)$ is 299 K. The lapse rate is given by

$$\frac{d\theta_a}{dz} = \begin{cases} 1 \ \ \text{K km}^{-1} & z < 1 \text{ km}, \\ 4 \ \ \text{K km}^{-1} & 1 \leq z \leq 10 \text{ km}, \\ 10 \text{ K km}^{-1} & z > 10 \text{ km}. \end{cases} \tag{1}$$

The surface value of the ambient pressure field $p_a(z)$ is 10^5 Pa. Above the surface, p_a is adjusted to ensure hydrostatic balance in a gravity field with g = 9.8 m s^{-2}. The constant thermal forcing varies with radius r and height z. For $z_b \leq z \leq z_t$, it is given by

$$\frac{d\theta}{dt} = \frac{\epsilon_\theta}{[1 + (r/r_\theta)^2]^2} \sin\left(\pi \frac{z - z_b}{z_t - z_b}\right), \tag{2}$$

in which ϵ_θ = 0.11 K s^{-1}, r_θ = 1 km, z_b = 1 km, z_t = 9 km, and $d\theta/dt$ is the material derivative of potential temperature. For $z < z_b$ or $z > z_t$, the thermal forcing is zero.

The initial cyclonic circulation (the parent vortex of the tornado) is confined to $z \leq z_m$ = 5 km, and approximately satisfies gradient balance. The azimuthal velocity distribution is given by

$$v = \frac{r/r_m}{1 + (r/r_m)^2} \sqrt{\frac{2B\theta_a z_m}{\pi} \left\{ \left[\cos\left(\frac{\pi z}{z_m}\right) + 1 \right] - \frac{1}{8} \left[\cos\left(\frac{2\pi z}{z_m}\right) - 1 \right] \right\}}, \tag{3}$$

in which r_m = 3 km and $B = 3 \times 10^{-4}$ m s^{-2} K^{-1}. A maximum wind speed of 12 m s^{-1} occurs on the surface at $r = r_m$. The radial velocity u and vertical velocity w are initially zero.

Of further note, the Coriolis parameter f is 10^{-4} s^{-1}, which is representative of 45^{o}N. Surface momentum fluxes are determined from the friction velocity for a logarithmic wind profile with neutral stability and a roughness length of 5 cm. The subgrid turbulence parameterization uses anisotropic Smagorinsky closure, and the aforementioned Rayleigh damping layer is applied above z = 15 km. Radiation conditions are enforced at the lateral boundaries of the outermost grid using the Klemp-Wilhelmson formula for waves traveling near 330 m s^{-1} [Klemp and Wilhelmson 1978].

With horizontal resolution down to a few meters on the innermost grid, the α-experiment (and others like it) took several weeks to complete on a modest 4-node cluster with a total of 32 processors. The importance of high resolution in simulating aeroacoustics (tornado infrasound in particular) is well documented [cf. S08; Colonius and Lele 2004]. Therefore, the relatively high computational cost was unavoidable, even after an extensive minimization effort.

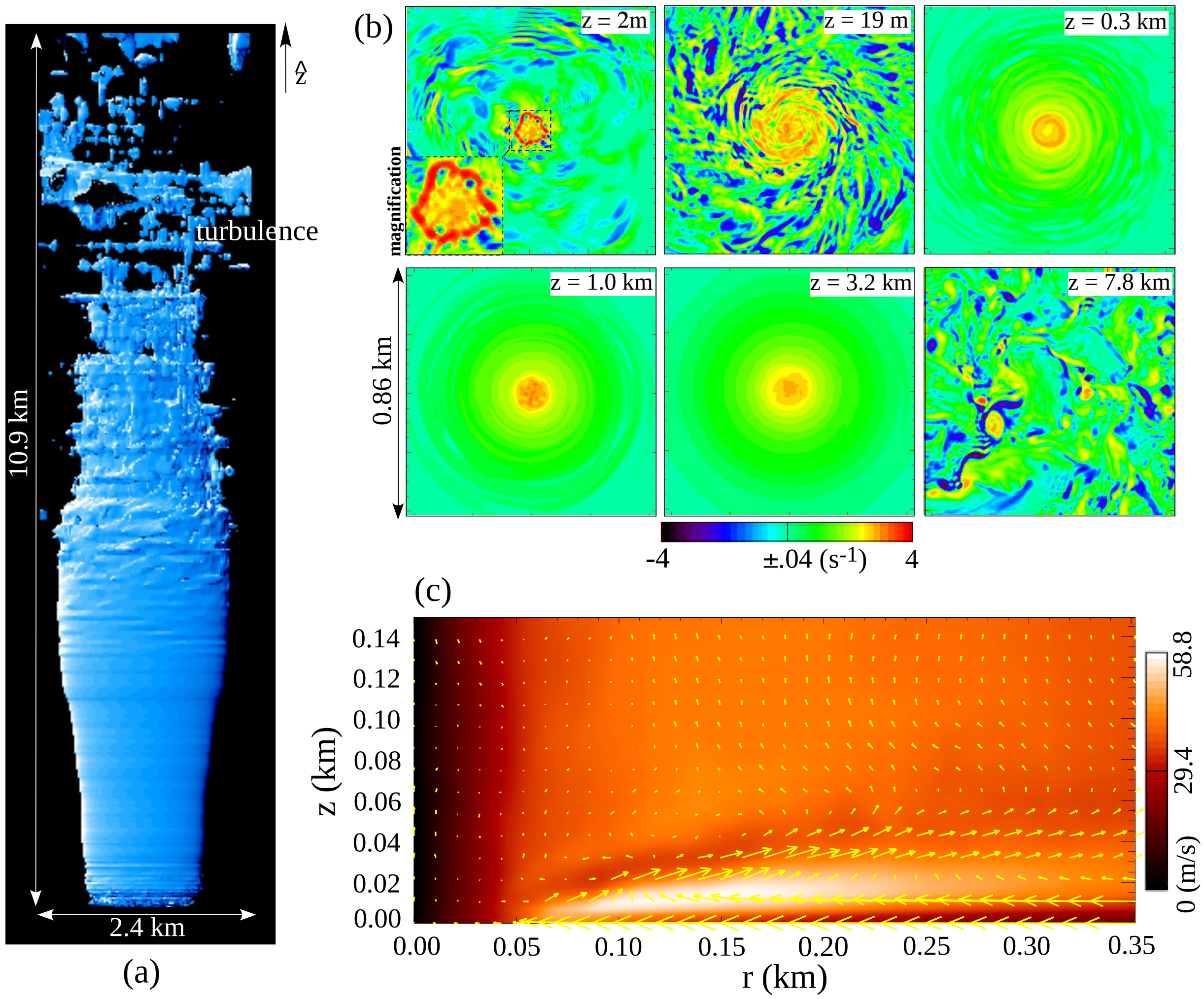

Figure 1: (color online) Basic structure of a simulated tornado driven by constant thermal forcing. (a) Isosurface of horizontal wind speed [$u_h(x, y, z)$] normalized to its z-dependent maximum $u_{max}(z)$; specifically, the isosurface corresponds to $u_h/u_{max} = 0.65$. (b) Vertical vorticity at 6 altitudes, smoothed with box-car averaging over 10.7 m in both horizontal dimensions (x and y). The positive and negative halves of the color scale are logarithmic and cover two orders of magnitude each. (c) Azimuthally averaged velocity field at the base of the tornado. Arrows show the secondary circulation, with a maximum wind speed of 32 m s^{-1}. The shading shows the azimuthal velocity. Panels (a) and (c) are snapshots at $t = 35$ min, whereas each panel in (b) is taken 10 s later.

3. Basic Tornado Structure in the C-RAMS Simulation

Figure 1 illustrates the mature tornado that develops after one-half hour in the α-experiment. Figure 1a shows an isosurface of the horizontal wind speed, normalized to its maximum value at a given altitude. Below $z = 5$ km, where the thermal forcing is peaked and the wind speed of the parent vortex becomes zero, the isosurface exhibits a funnel shape that is commonly associated with tornadoes. Above 7 km, the flow is turbulent. This upper turbulence appears to rely on the existence of a tornado, because it fails to develop inside the core of a non-tornadic updraft if the parent vortex is removed from the simulation [M.E. Nicholls, personal communication]. Figure 1b shows 6 horizontal slices of the vertical vorticity distribution ζ_z. The surface distribution is dominated by an unsteady ring with transient subvortices, which are here defined as prominent vorticity peaks [cf. Fiedler 1998; Lewellen et al. 2000]. The shape of the ring changes between elliptical and polygonal states on a time scale comparable to the surface rotation period of

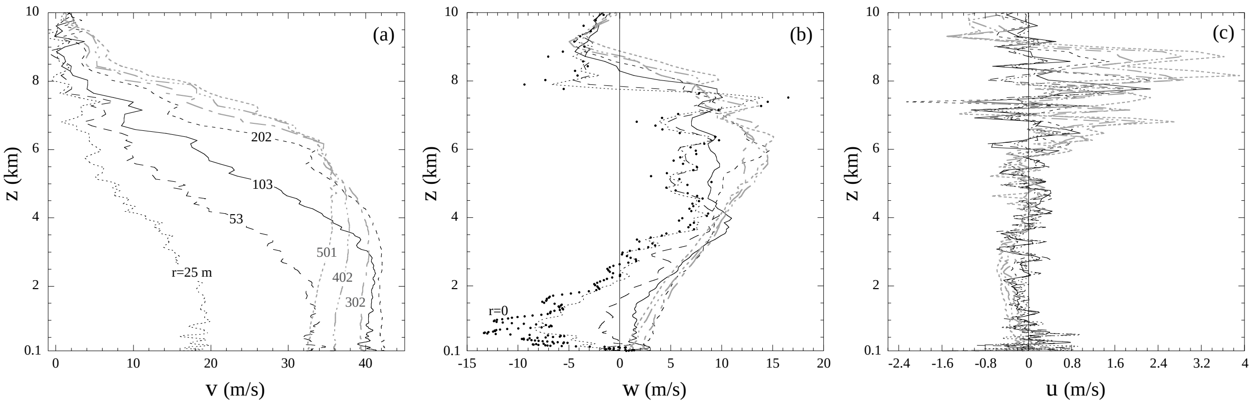

Figure 2: Azimuthally averaged wind profiles above the corner-flow region at $t = 35$ min in the α-experiment. (a) Azimuthal velocity. (b) Vertical velocity. (c) Radial velocity. The curve style varies with the value of the radial coordinate r. The specific values of r (in meters) are shown by the curve labels in (a) and (b).

the tornado. Ascending into the core,[2] the ring is replaced with a monotonic distribution. The transition to turbulence aloft is evident in the panel for $z = 7.8$ km. Figure 1c shows the azimuthally averaged velocity field at the base of the vortex. The peak azimuthal wind speed of 59 m s^{-1} occurs in a thin corner-flow region near the surface. The maximum radial inflow velocity is 32 m s^{-1} slightly above the surface.

Figure 2 shows the vertical variation of azimuthal velocity v, vertical velocity w and radial velocity u above the corner flow at $t = 35$ min. Each curve corresponds to the azimuthal average of v, w or u at a particular radius. The azimuthal velocity varies little with z over several kilometers of the lower troposphere. Vertical invariance of v in the outer core runs roughly twice as deep (5 km) as vertical invariance of v in the inner core. A prominent downdraft (region of negative w) occurs below $z \approx 2.5$ km along the central axis of the vortex. At $z = 0.62$ km, the interior downdraft has a peak value of 13 m s^{-1} and transitions to an updraft at $r = 66$ m. The radial velocity is predominantly negative in the lower troposphere and is predominantly positive aloft. The upper outflow velocity is an order of magnitude greater than the characteristic inflow velocity of the lower troposphere, but is an order of magnitude smaller than the inflow velocity near the surface (cf. Fig. 1c).

Figure 3a shows the radial variation of vertical vorticity ζ_z. Each curve corresponds to the azimuthal average of ζ_z at a select altitude in the lower troposphere. To a reasonable approximation, one may write

$$\zeta_z \approx \frac{\zeta_*}{1 + (r/r_v)^\gamma} \equiv Q\,(r; r_v, \zeta_*, \gamma)\,. \tag{4}$$

The z-dependent fit parameters (r_v, ζ_* and γ) are determined by the method of least squares. Figure 3b shows $\tilde{\zeta}_z \equiv \zeta_z/Q$ versus $\tilde{r} \equiv r/r_v$ for several values of z. Above 1 km, $\tilde{\zeta}_z$ stays close to unity for all $\tilde{r} \leq 5$. Figure 3c shows the vertical variation of the fit parameters. The radial length scale r_v of the vortex core increases from 57 to 151 m between $z = 1$ and 5 km. Over the same vertical interval, ζ_* decreases from 1.8 to 0.6 s^{-1}. On the other hand, γ stays fairly close to 1.8.

Evidently, the radial distribution of axial vorticity ζ_z is significantly non-Rankine. A Rankine vortex has constant ζ_z within a core radius r_v, and zero ζ_z outside. In other words, ζ_z is given by a Q-distribution [Eq. (4)] with $\gamma \to \infty$. By contrast, a Q-distribution with $\gamma = 1.8$ has a substantial skirt of monotonically decaying vorticity beyond r_v. The author believes that the presence of a monotonically decaying skirt is a realistic feature of the c-RAMS simulation. To begin with, radial diffusion of the vortex core (due to subgrid eddy-viscosity) has an estimated time scale 10 times greater than the 36 minute duration of the simulation. Furthermore, the structure of the skirt seems insensitive to a 56% reduction of Δ_x and the attendant reduction of horizontal diffusivity, which is proportional to Δ_x^2 (see Fig. 3a).

[2]The “vortex core” is ambiguously defined in the literature. Here, it refers to the central region of the vortex above the corner flow and below the turbulent outflow layer.

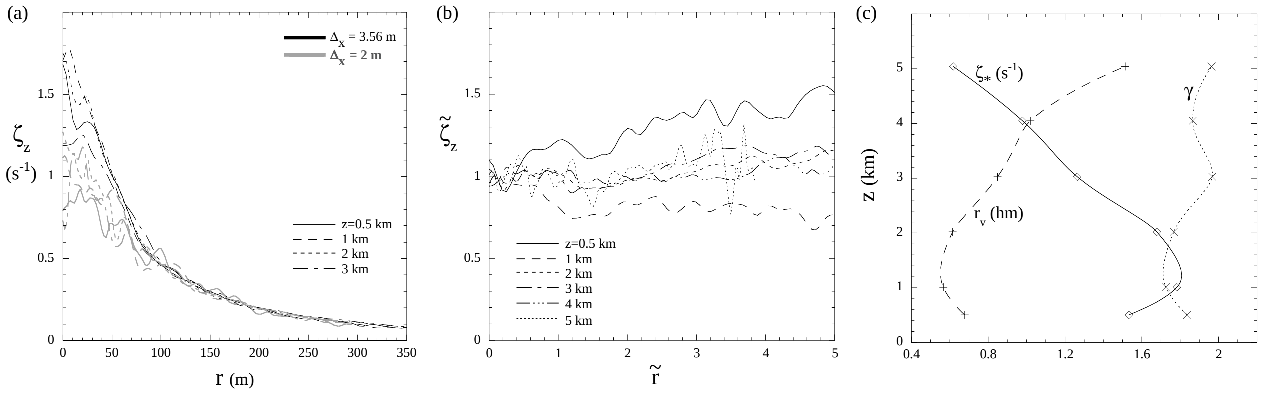

Figure 3: Vertical vorticity distribution ζ_z of the core at $t = 35$ min. (a) Azimuthally averaged ζ_z in the α-experiment and a similar numerical experiment where Δ_x is reduced to 2 m (8 m) and L is reduced to 612 m (1.6 km) on the innermost (second innermost) grid. (b) Azimuthally averaged ζ_z in the α-experiment normalized to best-fit Q-distributions *versus* radius normalized to r_v. (c) The fit parameters of the Q-distributions.

Details of the skirt may depend on details of both the parent vortex and the thermal forcing function. Nevertheless, a generic skirt seems qualitatively consistent with a large number of tornado and dust devil observations [e.g., Wood and White 2008; Bluestein et al. 2007; Tanamachi et al. 2007; Lee and Wurman 2005; Tratt et al. 2003].[3] The significance of a skirt to the production of infrasound will be addressed in section 6.

4. Simulated Infrasound

Figure 4 illustrates the infrasound generated in the α-experiment. The plotted fields are filtered pressure perturbations, defined by

$$p_f \equiv \overline{p}^{\tau_1} - \overline{\overline{p}^{\tau_1}}^{\tau_2}, \tag{5}$$

in which p is the total atmospheric pressure and

$$\overline{p}^{\tau}(\mathbf{x}, t) \equiv \frac{1}{\tau} \int_{t-\tau/2}^{t+\tau/2} d\tilde{t}\; p(\mathbf{x}, \tilde{t}). \tag{6}$$

Figure 4a is a 3D snapshot of p_f with $\tau_1 = 0$ and $\tau_2 = 10$ s, which represents all waves with frequencies greater than about 0.1 Hz.[4] In this frequency regime, one sees that infrasonic waves emitted from the upper turbulence have equal or greater intensity than emissions from the vortex core.

Figures 4b and 4c are Hovmöller plots of the ~0.1-1 Hz and $\gtrsim$0.5 Hz pressure perturbations. Specifically, the plots are of p_f with (τ_1, τ_2)=(1.2 s, 10 s) and (0, 2 s). The x-axis shows distance on a horizontal line cutting through the center of the system, at the altitude indicated on each plot. The dashed lines correspond to the x-t phase-trajectories of waves propagating at the speed of sound in the positive and negative x-directions. At large horizontal distances from the source, the phase-curves become parallel to the dashed lines. This confirms that the filtered pressure perturbation is acoustic radiation sufficiently far away from the driven vortex and the turbulent inflow/outflow regions. Closer to the central axis ($x = 0$), the dominant phase curves in the near-surface Hovmöller plots are horizontal. Such behavior is consistent with waves coming from centralized sources aloft.

Figure 5 is a typical time series of the simulated infrasonic pressure perturbation, minus its linear trend during an analysis period of $\tau = 40$ s. The detrended pressure perturbation is precisely defined by the following equation:

[3] It is worth noting that there are some cases in which Rankine wind structure (negligible ζ_z outside the radius of maximum wind) seems reasonably consistent with the data [e.g., Sinclair 1973; Bluestein et al. 2004; Bluestein 2005].

[4] The maximum frequency at which acoustic waves are resolved on a computational grid is $c/4\Delta$, in which c is the sound speed and Δ is the grid spacing. The coarse resolution of the largest grid (shown in Fig. 4a) does not permit the accurate representation of acoustic waves with frequencies greater than about 1 Hz.

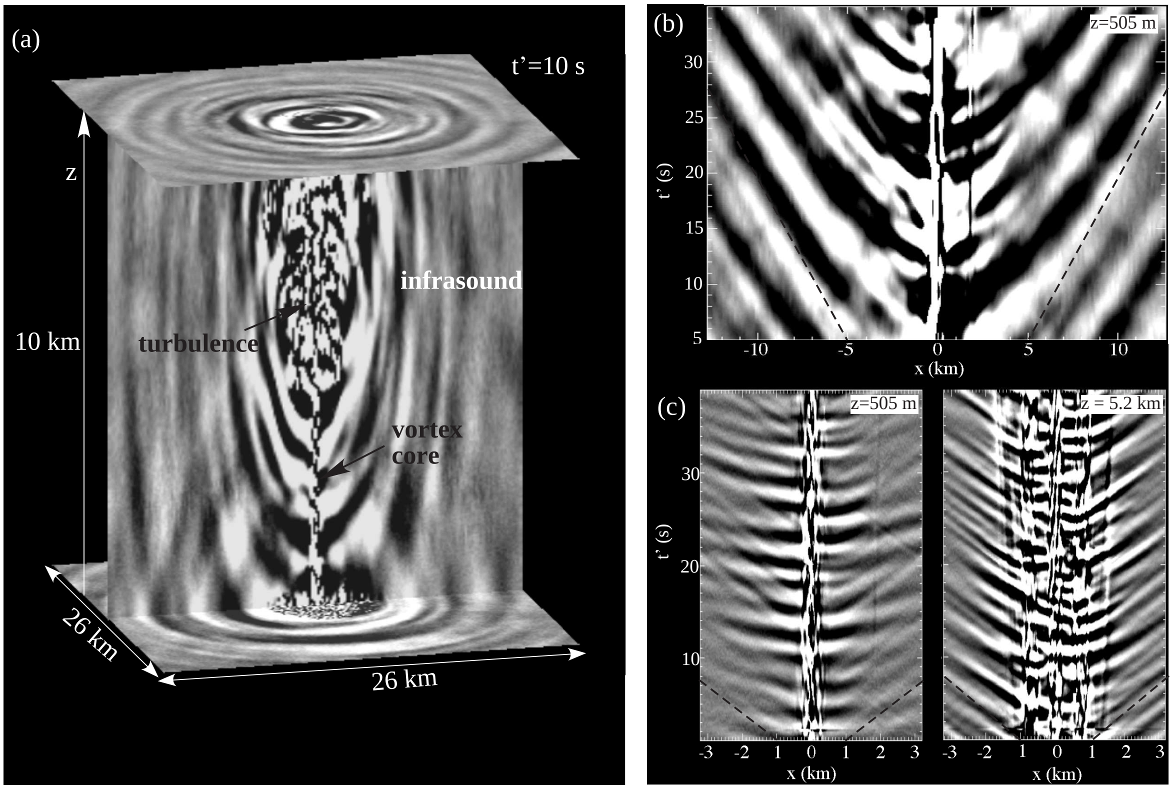

Figure 4: Infrasound generated in a thermally driven tornado simulation. (a) The filtered pressure perturbation showing all waves with frequencies greater than about 0.1 Hz. The outer waves constitute infrasonic radiation. (b) Hovmöller plot of the ~0.1-1 Hz pressure perturbation 505 m above the surface. (c) Hovmöller plots of the $\gtrsim$0.5 Hz pressure perturbation 505 m and 5.2 km above the surface. The greyscales are linear in all plots, with bright/dark shades representing positive/negative values. Positive/negative pressure anomalies exceeding 0.05 Pa in (a), 0.025 Pa in (b) or 0.1 Pa in (c) are mapped onto white/black. The time variable t' is zeroed at 35 min. The dashed lines in (b) and (c) are phase-trajectories for sound waves propagating parallel to the x-axis.

$p'_d \equiv p - [p_o + (p_\tau - p_o)t'/\tau]$, in which p_o and p_τ are the pressure fields evaluated at the beginning ($t' = 0$) and end ($t' = \tau$) of the analysis period. The time series is taken 0.5 km above ground, to avoid corruption by non-acoustic pressure fluctuations associated with near-surface turbulence in the weakly stratified boundary layer. The dashed and dotted curves show the 0.1-10 Hz and 0.5-2.5 Hz components of the signal. Both components are determined by standard Fourier analysis. [The detrended signal is continued to $t' = 2\tau = 80$ s with odd symmetry about the center ($t' = \tau$), and the Fourier transform is computed. Frequency components outside the band of interest are zeroed, and the inverse transform is calculated.] Figure 5 demonstrates that the detrended time-series has a peak frequency of order 0.1 Hz. The 0.5-2.5 Hz component, which is directly comparable to published field measurements [B05], is an order of magnitude smaller than the ~0.1 Hz waves. The preceding result has been verified for *all* computational point measurements (around thermally driven tornadoes) that will appear in section 5 of this paper. These include measurements from all but the innermost grid, and from a simulation with reduced Δ_z and greater resolution of high frequency waves in the upper troposphere.

The magnitude of the simulated infrasound does not obviously exceed scale estimates for noise generated adiabatically by the upper level turbulence [cf. Lighthill 1952; Proudman 1952; Meecham and Ford 1958, Stein 1967; Howe 2003]. However, such estimates have large uncertainties, and are more useful in efforts to understand the basic scaling of acoustic power with the turbulent Mach number in a broader set of numerical experiments. Moreover, other acoustic sources are conceivable in a dry c-RAMS simulation, such as parameterized diffusion of potential temperature. Appendix A provides further discussion of the possibilities. It is worth noting that high frequency ($\gtrsim$ 1 Hz) acoustic

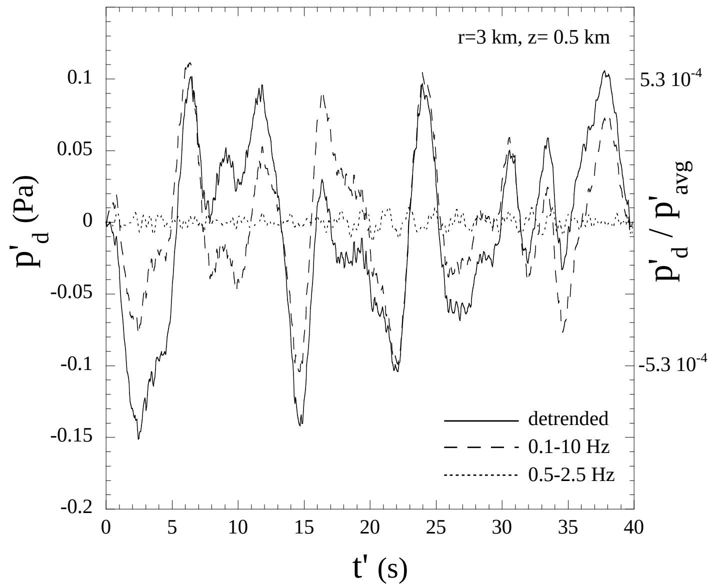

Figure 5: Time series of the linearly detrended pressure perturbation p'_d at a grid point where r = 3 km and z = 0.5 km. The dashed curve is the 0.1-10 Hz component of p'_d, whereas the dotted curve is the 0.5-2.5 Hz component. The right axis shows the scale of p'_d normalized to the local pressure perturbation of the atmosphere averaged over the analysis period [$p'_{avg} \equiv \int_0^\tau dt'(p - p_a)/\tau$, in which τ = 40 s].

radiation from the upper level turbulence could be tainted by spurious emissions at the boundary of the innermost grid. The reader may consult appendix B for a more detailed description of this potential problem. With limited computational resources, it was impractical to cover the multi-kilometer domain of upper level turbulence with a single fine grid. While this brings into question the accuracy of the simulated high frequency radiation, there was no obvious tainting of low frequency ($\lesssim$ 0.1 Hz) emissions.

5. Significance of the Simulation Results

Regardless of what sources contribute to the computed infrasound, it is relatively weak. To see this, let us compare its magnitude to that of the infrasound generated by other c-RAMS simulations and observed thunderstorms.

Figure 6 shows the peak-to-peak amplitude of the infrasonic pressure perturbation versus distance from the center of the source in a variety of c-RAMS simulations. Unless stated otherwise, the plotted amplitude is obtained (after Fourier analysis) from the 0.1-10 Hz component of the near-surface pressure perturbation, which is dominated by contributions near 0.1 Hz. Solid squares correspond to the α-experiment. Small empty squares correspond to a similar numerical experiment that uses a modified vertical grid. The modified grid is uniformly spaced (with Δ_z = 40 m) for $z \leq 8$ km and moderately stretched (with $\Delta_z < 100$ m) for $8 \leq z \leq 10$ km. Large empty squares correspond to another variant of the α-experiment that uses a slightly wider innermost grid (with L = 1.4 km) and an isotropic Smagorinsky parameterization of subgrid turbulence. The isotropic turbulence parameterization sets the diffusivity proportional to Δ_z^2 for all directions, thereby weakening wind fluctuations and their acoustic emissions at high altitudes where Δ_z is large.[5] Solid diamonds represent the 0.05-0.5 Hz component of the pressure perturbation in the α-experiment.

For comparison, the grey triangles in Fig. 6 show computed amplitudes of the ~0.1 Hz infrasound of a mature, non-rotating cumulonimbus simulated with c-RAMS. The reader may consult S08 for details of the computational setup.

[5]The diffusivity associated with subgrid turbulence depends not only on grid-spacing and the local deformation rate, but is directly proportional to the dimensionless tuning-parameter $C_{x,z}^2$ [see the RAMS Technical Manual and Namelist Documentation available at www.atmet.com]. The value of $C_{x,z}$ is set equal to 0.25 in the α-experiment, 0.25 in the experiment with constant Δ_z below 8 km, and 0.15 in the experiment with isotropic diffusivity.

Notably, Δ_x =30 m for the innermost grid (which nearly covers the entire cloud) and Δ_z is continuously stretched from 5 to 74 to 233 m at altitudes of 5 m, 3 km and 10 km, respectively. Downward and upward pointing triangles correspond to simulations with 1-moment and 2-moment microphysics parameterizations [Walko et al. 1995,2000; Meyers et al. 1997; Saleeby and Cotton 2004]. In both cases, the infrasound comes from diabatic processes in the hail-to-rain transition layer [S11]. The grey sidebar on the right-hand side of the plot indicates the level of 0.5-2.5 Hz infrasound that might be expected within 20 km of a tornadic thunderstorm, as inferred from published observations [Fig. 4 of B05].

The grey circles in Fig. 6 show computed amplitudes of the sustained ~0.1 Hz acoustic emissions of 3D VR waves propagating azimuthally around the cores of non-convective Rankine vortices. These simulation data (which are obtained using a distinct measurement technique) are taken directly from S08. The solid and empty grey circles correspond to vortices with 100 m s^{-1} and 50 m s^{-1} maximum surface velocities (respectively) at r_v = 100 m. Both vortices have 6 km vertical decay lengths. Precisely stated, $\zeta_z \propto e^{-z/z_v}$ with $z_v = 6$ km. The solid black circles represent the infrasound of a 3D VR wave on a Rankine vortex resembling (in size and intensity) the *core* of the vortex generated in the α-experiment.[6] The maximum surface velocity of the α-like vortex is 38 m s^{-1} at r_v = 75 m, and the vertical decay length z_v is 4.5 km. The vertical variation of the α-like vortex differs from that of the S08 vortices, in that

$$\zeta_z \propto \frac{1}{1 + (z/z_v)^{4.5}} \equiv Z\,(z; z_v)\,. \tag{7}$$

In both the grey and black simulations, the VR waves are initialized by imposing vertically uniform, quasi-balanced, elliptical deformations of the vortex core [see appendix D of S08]. The perturbation strength is measured by the maximum fractional displacement ϵ of the azimuthally dependent core radius from its unperturbed value r_v. The grey simulations have $\epsilon = 0.1$, whereas the black simulation has $\epsilon = 0.2$. All of the VR wave simulations are without surface drag and take place under isothermal ambient conditions, in which the temperature T_a is 300 K. Of further note, it has been verified that the infrasound generated by VR waves in c-RAMS is consistent with classic vortex sound theory [S08; S11].

Consideration of Fig. 6 leads to the following tentative conclusions:

- The wind fluctuations of an ordinary tornado (as that of the α-experiment) do not readily produce ~0.1 Hz acoustic emissions that are discernible from those of diabatic cloud processes.

- The 0.5-2.5 Hz emissions, which have much smaller magnitude according to Fig. 5, could not account for the observed infrasound of a tornadic thunderstorm.

- The cores of dry, thermally driven tornadoes do not radiate as strongly as they could in the 0.1 Hz frequency regime, by comparison to less realistic numerical experiments with Rankine vortices.

The validity of the preceding inferences should be viewed as contingent upon verification with substantially finer grids and (with regard to the top bullet) refined microphysics parameterizations, once such verification becomes practical. Nevertheless, the quiet core observed in our simulations is an especially interesting result that seems to have a very reasonable explanation.

6. The Quiet Core

There are two notable reasons why the vortex core is relatively quiet in the simulations. First, the structure of the core inhibits asymmetric deformations associated with VR waves. Second, the principal axisymmetric oscillations (axisymmetric Kelvin modes) of a columnar vortex are non-radiative.

[6] Figures 7a-7c of section 6 show the perturbed vortex that generates the infrasound represented by the solid black circles.

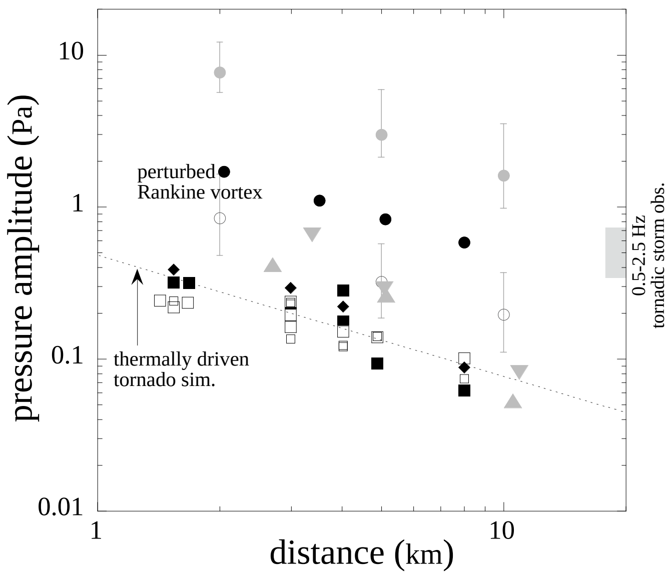

Figure 6: Infrasonic pressure perturbation near the surface *versus* distance from the center of the source. **Squares and Diamonds:** the ~0.1 Hz infrasound produced in thermally driven tornado simulations with various grid configurations and subgrid turbulence parameterizations. The dotted line through these data points is to aid the eye. See text for details. **Triangles:** the ~0.1 Hz infrasound of a simulated non-rotating cumulonimbus with 1-moment (downward pointing) and 2-moment (upward pointing) microphysics parameterizations [cf. S08]. **Circles**: the ~0.1 Hz infrasound generated by VR waves in the cores of Rankine vortices with finite depth. The solid and empty grey circles (with error bars) are for the S08 vortices with maximum wind speeds of 100 m s^{-1} and 50 m s^{-1}, respectively. The solid black circles are for a vortex with a maximum wind speed of 38 m s^{-1}, a vertical structure closer to a thermally driven tornado, and a VR wave with twice the amplitude of the others.

6.1. *Structural Resistance to Asymmetric Deformations Associated with VR Waves*

Section 3 showed that our thermally driven tornado has a substantial skirt of monotonically decaying vorticity beyond the radius r_v. It is well known (in the context of 2D perturbation theory) that wave-flow resonances in a monotonically decaying skirt can severely damp quasi-discrete VR waves [Briggs et al. 1970; Schecter et al. 2000; S08]. Section 3 also showed that the vorticity distribution has a gradual transition from high to low values between the inner and outer core. A gradual transition, as opposed to a step at r_v, allows arbitrary asymmetric perturbations to project more strongly onto radially sheared VR waves than onto quasi-discrete VR waves [Schecter 1999]. Perturbations consisting of radially sheared VR waves exhibit spiral wind-up of vorticity, and their pressure fields typically decay at the characteristic shear-rate of the differential rotation.[7] It stands to reason that neither sheared nor quasi-discrete VR waves, in the core of the thermally driven tornado, are likely to persist and generate sustained infrasound. Moreover, their propensity to decay suggests a tendency to resist excitation.

A pair of simple simulations clearly illustrates how the non-Rankine monotonic structure of ζ_z can suppress infrasonic emissions. Figure 7 shows the evolution of two elliptically deformed vortices. Both vortices have basic states of the form $\zeta_z = Q(r; r_v, \zeta_*, \gamma)Z(z; z_v)$, in which $r_v = 75$ m and $z_v = 4.5$ km. The functions Q and Z are defined by Eqs. (4) and (7), respectively. The top vortex has Rankine structure, characterized by $\gamma = \infty$ and $\zeta_* = 1.07$ s^{-1}. The bottom vortex has greater resemblance to that of the α-experiment, in that $\gamma = 1.8$ and $\zeta_* = 1.45$ s^{-1}. Both deformed vortices are in nonlinear balance without secondary circulation at $t = 0$ [cf. appendix D of S08]. Figures 7a and 7d show the initial conditions near the surface. The phase of the initial elliptical perturbation does not vary with z. The ambient state of the atmosphere is isothermal (with $T_a = 300$ K) and the Coriolis parameter is zero. The hydrostatically balanced pressure field p_a is 10^5 Pa on the surface.

The computational configuration is the same for both simulations. The nested horizontal grids are identical to those of the α-experiment. On the other hand, the vertical mesh has uniform spacing ($\Delta_z = 178.2$ m) and extends to $z = 18$

[7] Needless to say, it is theoretically possible for transient growth to precede decay [Schecter 1999; Nolan and Farrell 1999; Antkowiak and Brancher 2004].

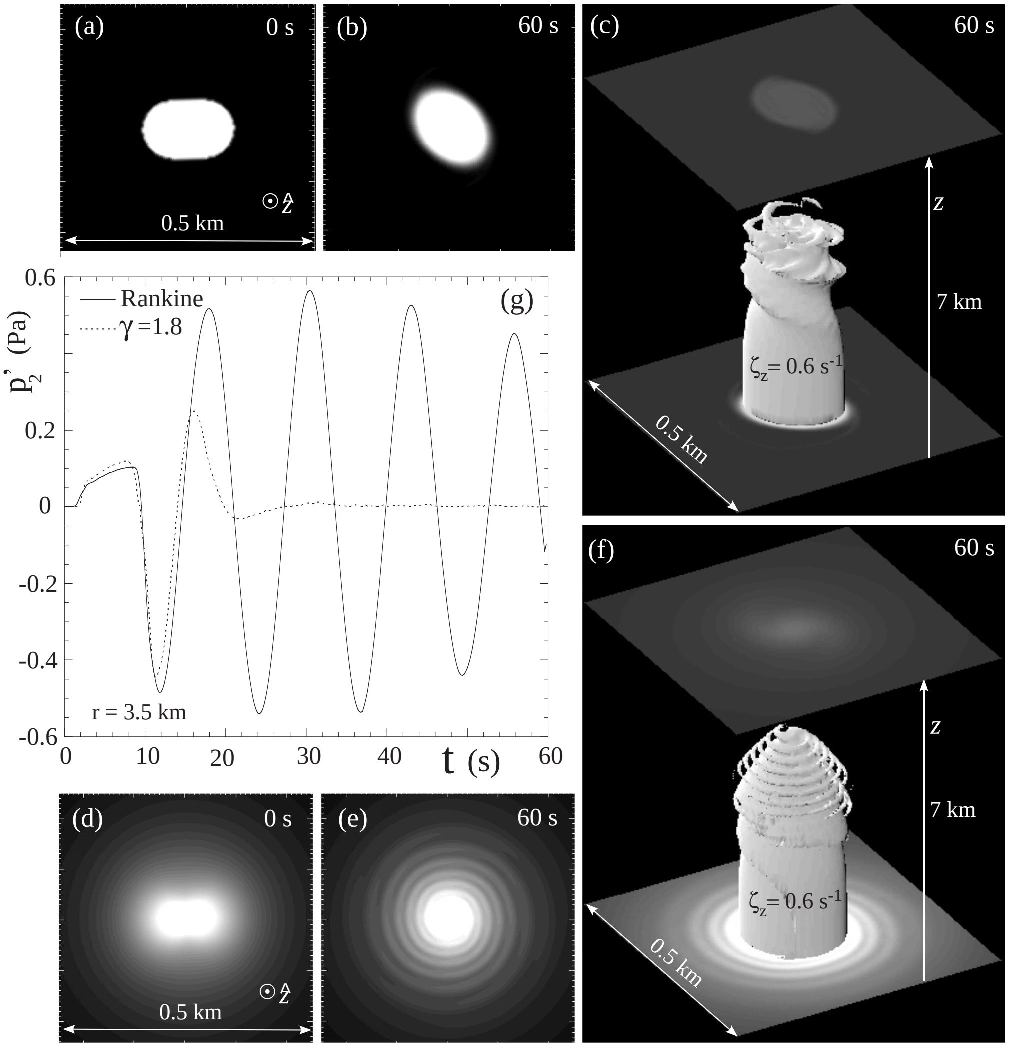

Figure 7: Vortex Rossby waves and their infrasound in two simple c-RAMS simulations. Plots (a-c) illustrate the evolution of ζ_z for a vortex with $\gamma = \infty$ (Rankine structure) and vertical variation similar to that of the core of a thermally driven tornado. The phase of the elliptical asymmetry ($n = 2$ VR wave) is initially invariant with z. Plots (d-f) illustrate the evolution of ζ_z for a vortex with $\gamma = 1.8$ and a similar initial disturbance. Plots (a,b,d,e) show horizontal slices of ζ_z near the ground ($z = 89$ m) at $t = 0$ and 60 s. The greyscale ranges from $\zeta_z = 0$ (black) to $\zeta_z = 1$ s^{-1} (white). Lesser or greater values are mapped onto black or white, respectively. Plots (c,f) are 3D visualizations of the perturbed vortices at $t = 60$ s. The isosurfaces correspond to $\zeta_z = 0.6$ s^{-1}. The greyscales of the horizontal contour plots range from $\zeta_z = 0$ to $\zeta_z = 0.5$ s^{-1}. Plot (g) shows the $n = 2$ Fourier component of the near-ground infrasonic pressure perturbation ($p'_2 \equiv \hat{p}'_2 e^{i2\varphi} + c.c.$) at $r = 3.5$ km. Inviscid damping of the core VR wave (axisymmetrization) strongly inhibits the production of infrasound for $\gamma = 1.8$.

km (as opposed to 28 km). The vertical resolution may seem coarse, but Δ_z is small compared to the characteristic vertical wavelengths of the simulated VR waves and their acoustic emissions. Surface momentum fluxes are set to zero, but the subgrid turbulence parameterization otherwise matches that of the α-experiment.

During a 60 s time interval, the elliptical deformation of the Rankine core propagates counter-clockwise with minimal decay. S08 verifies, for a similar numerical experiment, that the propagating disturbance has the characteristics of an $n = 2$ VR wave, in which n is the azimuthal wavenumber. The phase speed of the VR wave varies with height (most dramatically above z_v) due to vertical shear in the basic state. This results in the twisted vorticity isosurface that is shown in Fig. 7c. In contrast to the virtually undamped VR wave of the Rankine vortex [Figs. 7a-7c], the elliptical deformation of the non-Rankine vortex decays rapidly with time [Figs. 7d-7f].

Figure 7g shows near-surface time series of the infrasound generated by the Rankine and non-Rankine vortices. Specifically, each curve corresponds to the dominant $n = 2$ component of the following Fourier expansion of the infrasonic pressure perturbation:

$$p' = \hat{p}'_0(r,z,t) + \sum_{n=1}^{\infty} \left[\hat{p}'_n(r,z,t) e^{in\varphi} + c.c. \right], \tag{8}$$

in which φ is the azimuthal angle of the vortex-centered cylindrical coordinate system, and $c.c.$ denotes the complex conjugate of the preceding term. While the infrasound of the Rankine vortex persists, that of the non-Rankine vortex decays to a small fraction of its initial amplitude after one oscillation period.

It should be noted that sheared and quasi-discrete VR waves do not form a complete basis of asymmetric ($n \neq 0$) perturbations in a 3D columnar vortex [Alekseenko et al. 2007; Fabre et al. 2006; Saffman 1992]. The excitation of non-VR modes was greatly reduced in the simple simulations of this section by enforcing quasi-2D nonlinear balance at $t = 0$. The present focus on VR waves is partly justified by an earlier paper that advocated their potential relevance to the infrasound emitted by tornadoes [S08]. A comprehensive explanation for the weak infrasound (at 0.1-1 Hz) created by more general asymmetric disturbances in the core of the thermally driven tornado would be exhaustive, and is best deferred to a separate theoretical paper.

6.2. Non-Radiative Nature of the Principal Axisymmetric Vortex Modes

On the other hand, it is important to briefly address the insignificant emissions from axisymmetric ($n = 0$) disturbances. Bedard proposed that the 0.5-10 Hz infrasound emitted by a severe storm is primarily generated by axisymmetric oscillations of a tornado or pre-tornado vortex [B05]. This interpretation was based on the untested theoretical work of Abdullah [1966]. A more recent linear analysis clarified that the principal axisymmetric oscillations of a subsonic, columnar vortex (axisymmetric Kelvin modes) can not excite acoustic radiation [Schecter 2012]. Numerical experiments further showed that (as in free space) axisymmetric radiation is shaped primarily by the impulse that triggers the emission, not by the properties of the vortex [ibid]. It seems reasonable to infer that a significant level of axisymmetric radiation from the vortex core would require a supplementary acoustic source that is absent from the c-RAMS simulations considered here.

7. Conclusion

The preceding sections described the infrasound of a non-supercell tornado that was driven by an artificial buoyancy source in the dry dynamical core of c-RAMS. Despite strong fluctuations in the lower corner flow and upper outflow regions, the infrasound of the tornado was surprisingly weak. In the 0.1 Hz frequency regime, the infrasound was no stronger than that of a simulated, non-rotating cumulonimbus. The smooth, skirted core of the tornado was partly responsible for this, as it was shown to suppress VR waves and their infrasonic radiation fields. In the 0.5-2.5 Hz frequency regime, the infrasound of the tornado (plus grid noise contamination) was at least an order of magnitude weaker than the infrasound observed to emanate from a severe storm.

While somewhat disconcerting, the preceding results should not be seen to refute the compelling reports of discernible infrasound emitted by tornadoes [B05]. First note that the tornado simulations in this paper neglected all thermal fluctuations associated with phase-transitions of cloud moisture. Conceivably, the presence of an intense convective vortex could amplify the thermal fluctuations and their acoustic emissions [cf. Nicholls et al. 2004]. The simulations also neglected the influence of debris on the structure and oscillations of the tornado [Lewellen et al. 2008]. Static thermal forcing in a shear-free environment was another unrealistic feature of the simulations. This particular setup kept the vortex nearly erect, and reduced perturbations that might have developed by quasi-steady translation over a frictional surface. In principle, more realistic simulations could provide a mechanism for ordinary tornadoes to generate discernible infrasound, but this mechanism will have to await future discovery. If fine-scale turbulence is an essential component of the prevailing mechanism, then definitive computational studies may require substantially higher resolution than was used for this study.

Acknowledgments

The author duly acknowledges the contributions of Dr. Melville E. Nicholls in conducting the thermally driven tornado simulations that were analyzed for this paper. Dr. Nicholls was behind the decision to use θ-forcing in a stably stratified atmosphere, as opposed to w-forcing in a neutral atmosphere [cf. Fiedler 1998]. Moreover, he selected the specific stratification profile [Eq. (1)], forcing function [Eq. (2)], and wind profile of the parent vortex [Eq. (3)]. With regard to more technical matters, Dr. Nicholls simplified the surface-layer parameterization of c-RAMS [cf. Louis 1979] to one in which the vertical momentum-flux is obtained from the friction velocity of a logarithmic wind profile with neutral stability and a roughness length of 5 cm. Furthermore, at the request of the author, he removed several nonlinear switches from the anisotropic diffusion scheme of c-RAMS that might have otherwise created spurious infrasound. Finally, Dr. Nicholls tuned the run-time parameters of the diffusion scheme to reduce grid noise in the bottom inflow layer, without excessively decreasing the effective Reynolds number.

This work was supported by the National Science Foundation (NSF), under grant AGS-0832320. The cumulonimbus simulation with 2-moment microphysics was carried out on the Steele supercomputer at Purdue University, which is part of NSF TeraGrid.

Appendix A. Acoustic Sources in C-RAMS

An acoustic source is rigorously defined as a term on the right-hand side of an inhomogeneous acoustic wave equation (AWE). Schecter [S11] constructed the following AWE from the fundamental equations of c-RAMS [cf. Akhalkatsi and Gogoberidze 2009,2011]:

$$\partial_{tt}\Pi' - \frac{c_a^2}{\rho_a\theta_{va}^2}\partial_i\left(\rho_a\theta_{va}^2\partial_i\Pi'\right) = S_m + S_{uu} + S_{pu} + S_b + S_c + S_{tb}, \tag{A.1}$$

in which

$$\begin{aligned} S_m &\equiv \partial_t\left(\frac{c^2}{\theta_v^2}\frac{d\theta_v}{dt} + \frac{c^2}{\theta_v(1+q_v)}\frac{dq_v}{dt}\right), & S_{uu} &\equiv \frac{c_a^2}{\rho_a\theta_{va}^2}\partial_i\left(\rho_a\theta_{va}u_j\partial_j u_i\right), \\ S_{pu} &\equiv -\partial_t\left(u_i\partial_i\Pi' + \frac{R}{c_v}\Pi'\partial_i u_i\right), & S_b &\equiv -\frac{c_a^2}{\rho_a\theta_{va}^2}\partial_3\left\{g\rho_a\left[\theta_v' - \theta_{va}(q_t - q_v)\right]\right\}, \\ S_c &\equiv -\frac{c_a^2}{\theta_{va}}\partial_i(\varepsilon_{ij3}fu_j), & S_{tb} &\equiv -\frac{c_a^2}{\rho_a\theta_{va}^2}\partial_i\left(\rho_a\theta_{va}\partial_j\sigma_{ij}\right). \end{aligned} \tag{A.2}$$

Here, $\Pi \equiv c_p(p/p_{ref})^{R/c_p}$ is the Exner function, p is total pressure, $p_{ref} = 10^5$ Pa, ρ is the mass density of the gaseous component of moist air, $\theta_v \equiv c_p p/R\rho\Pi$ is the virtual potential temperature, $c^2 \equiv R\Pi\theta_v/c_v$ is (basically) the local sound speed, g is gravitational acceleration, and f is the Coriolis parameter. R, c_p and c_v are the gas constant and specific heats (at constant pressure and volume) of air. The variables q_t and q_v are the total and vapor mixing ratios of water substance. The variable u_i is the i^{th} Cartesian component of the velocity field, and σ_{ij} is the viscous stress tensor associated with small-scale turbulence. The symbol ∂_i is shorthand for the partial derivative with respect to the Cartesian coordinate x_i, and $d/dt \equiv \partial_t + u_i\partial_i$ is the material derivative. The Einstein convention is used for summation where i or j is repeated. An a-subscript or prime denotes an ambient or perturbation field. Ambient fields depend only on the vertical coordinate x_3, which is equivalent to z of the main text.

Each term on the right-hand side of Eq. (A.1) can be viewed as a localized acoustic source, due to its smallness (compared to the left-hand side) in the radiation zone of high frequency infrasound [S11]. The first term S_m is usually connected to heat and mass production by phase transitions of moisture. In the thermally driven tornado simulations, q_v is zero and the heat source [Eq. (2) with $\theta = \theta_v$] is static. Nevertheless, it is conceivable that parameterized diffusion could activate high frequency components of $d\theta_v/dt$, and c^2/θ_v^2 could exhibit high frequency Eulerian fluctuations. Therefore, it is conceivable that S_m could be nonzero in the infrasonic frequency band of interest.

The second term S_{uu} reduces to Lighthill's quadrupole source of acoustic radiation in a dry isentropic atmosphere with negligible gravity and uniform ρ_a [Lighthill 1952]. Following Powell 1964, it is readily converted into an

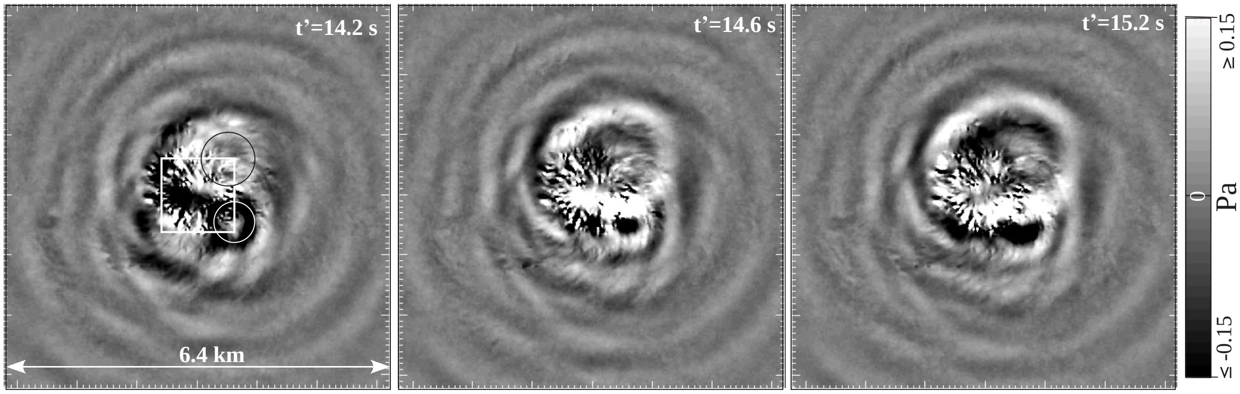

Figure B.1: Snapshots of the frequency filtered infrasound at z = 7.3 km, showing waves with frequencies $\gtrsim$1 Hz. The circles in the far left plot are approximately concentric with wave fronts that appear to emanate from the boundary of the innermost grid (white square).

expression whose most influential term is proportional to the divergence of the cross-product of vorticity and velocity [cf. S11]. The prevailing term is commonly identified as the source of vortex sound [Howe 2003]. Schecter [S11] describes in detail how S_{uu} is responsible for the infrasound of 3D VR waves that propagate around the cores of tornado-like vortices.

Scale estimates pertaining to real storms suggest that the infrasound of S_{uu} (associated with a tornado) or S_m (associated with moist cloud turbulence) should dominate the infrasound of all other sources in Eq. (A.1) [S11]. An additional source term,

$$S_{p\theta} \equiv \frac{c_a^2}{\rho_a \theta_{va}^2} \partial_i (\rho_a \theta_{va} \theta_v' \partial_i \Pi'), \tag{A.3}$$

would appear on the right-hand side of Eq. (A.1) if c-RAMS did not neglect the acceleration due to $-\theta_v' \partial_i \Pi'$ in the momentum equation. In theory, the infrasound of S_m associated with phase transitions of moisture (such as condensation induced by turbulent mixing) dominates that of $S_{p\theta}$ [AG09; S11]. Therefore, neglecting $S_{p\theta}$ is a relatively minor limitation of the present study, compared to neglecting phase transitions of moisture.

While possible, there is no need to laboriously compare the infrasound generated by each acoustic source term in the thermally driven tornado simulations of the main text. The outcome would be tangential to the main point of this paper, which is that the simulated infrasound is substantially weaker than expected from earlier theoretical studies and tornadic thunderstorm observations. During the next phase of simulations, which will include moisture and thereby better reflect reality, a rigorous assessment of each acoustic source may be more valuable [cf. S11].

Appendix B. A Subtle Numerical Issue

Section 4 alluded to a numerical issue with c-RAMS, concerning the artificial generation of high frequency infrasound at the boundary of a nested grid. Figure B.1 shows snapshots of p_f (with $\tau_1 = 0$ and $\tau_2 = 1$ s) in the α-experiment. The horizontal slices are taken near the base of the turbulent outflow, at z = 7.3 km. The square on the first plot shows the boundary of the innermost grid. The prominent, high frequency waves shown by p_f appear to emanate from this boundary.

In principle, one might reduce spurious emissions from the innermost grid boundary by extending that boundary well beyond the domain of turbulent flow. Alternatively, one might use a continuously stretched or adaptive grid. The former solution is impractical without massive computational resources, and the latter solution is not possible with c-RAMS. Nevertheless, accurate simulations of high frequency sound waves generated by severe weather will require some answer to this apparent problem.

References

Abdullah, A.J., 1966. The “musical” sound emitted by a tornado. *Mon. Weather Rev.*, **94**: 213-220.

Akhalkatsi, M., and G. Gogoberidze, 2009. Infrasound generation by tornadic supercell storms. *Q. J. Roy. Meteor. Soc.*, **135**: 935-940.

Akhalkatsi, M., and G. Gogoberidze, 2011. Spectrum of infrasound radiation from supercell storms. *Q. J. Roy. Meteor. Soc.*, **135**: 229-235.

Alekseenko, S.V., P.A. Kuibin and V.L. Okulov, 2007. *Theory of concentrated vortices.* Springer, N.Y., 492 pp.

Antkowiak, A. and P. Brancher, 2004. Transient energy growth for the Lamb-Oseen vortex. *Phys. Fluids*, **16**: L1-L4.

Bedard, A.J., Jr., 2005. Low-frequency atmospheric acoustic energy associated with vortices produced by thunderstorms. *Mon. Weather Rev.*, **133**: 241-263.

Bedard, A.J., Jr., B.W. Bartram, A.N. Keane, D.C. Welsh and R.T. Nishiyama, 2004. The infrasound network (ISNet): Background, design, details and display capability as a 88D adjunct tornado detection tool. *22nd Conference on Severe Local Storms*, Amer. Meteo. Soc., paper 1.1.

Bluestein, H.B., C.C. Weiss and A.L. Pazmany, 2004. Doppler radar observations of dust devils in Texas. *Mon. Wea. Rev.*, **132**: 209-224.

Bluestein, H.B., 2005. A review of ground-based, mobile, W-band Doppler-radar observations of tornadoes and dust devils. *Dyn. Atmos. Oceans*, **40**: 163-188.

Bluestein, H.B., C.C. Weiss, M.M. French, E.M. Holthaus, R.L. Tanamachi, S. Frashier and A.L. Pazmany, 2007: The structure of tornadoes near Attica, Kansas, on 12 May 2004. High-resolution, mobile, Doppler radar observations. *Mon. Wea. Rev.*, **135**: 475-506.

Bowman, H.A., and A.J. Bedard, 1971: Observations of infrasound and subsonic pressure disturbances related to severe weather. *Geophys. J. Roy. Astron. Soc.*, **26**, 215-242.

Briggs, R.J., J. D. Daugherty, and R. H. Levy, 1970. Role of Landau damping in crossed-field electron beams and inviscid shear flow. *Phys. Fluids*, **13**: 421-432.

Colonius, T.C., and S.K. Lele, 2004. Computational aeroacoustics: progress on nonlinear problems of sound generation. *Prog. Aerospace Sci.*, **40**: 345-416.

Cotton, W.R., R.A. Pielke Sr., R.L. Walko, G.E. Liston, C.J. Tremback, H. Jiang, R.L. McAnelly, J.Y. Harrington, M.E. Nicholls, G.C. Carrio and J.P. McFadden, 2003. RAMS 2001: Current status and future directions. *Meterol. Atmos. Phys.*, **82**: 5-29.

Fabre, D., D. Sipp, and L. Jacquin, 2006. Kelvin waves and the singular modes of the Lamb–Oseen vortex. *J. Fluid. Mech.*, **551**: 235-274.

Fiedler, B.H., 1998. Wind-speed limits in numerically simulated tornadoes with suction vortices. *Q. J. Roy. Meteor. Soc.*, **124**: 2377-2392.

Georges, T.M., 1976. Infrasound from convective storms. Part II: A critique of source candidates. *NOAA Tech. Rep. ERL 380-WPL 49*, 59 pp. [Available from the National Technical Information Service, 5285 Port Royal Rd. Springfield, VA 22161.]

Georges, T.M. and G.E. Greene, 1975. Infrasound from convective storms: Part IV. Is it useful for warning? *J. Appl. Meteor.*, **14**: 1303-1316.

Grasso, L.D., and W.R. Cotton, 1995. Numerical simulation of a tornado vortex. *J. Atmos. Sci.*, **52**: 1192-1203.

Howe, M.S., 2003. *Theory of Vortex Sound.* Cambridge Univ. Press, Cambridge, 216 pp.

Klemp, J.B., and R.B. Wilhelmson, 1978. The simulation of three-dimensional convective storm dynamics. *J. Atmos. Sci.*, **35**: 1070-1093.

Lee, B.D., and R.B. Wilhelmson, 1997. The numerical simulation of non-supercell tornadogenesis. Part I: Initiation and evolution of pretornadic misocyclone circulations along a dry outflow boundary. *J. Atmos. Sci.*, **54**: 32-60.

Lee, W.-C., and R.B. Wurman, 2005. Diagnosed three-dimensional axisymmetric structure of the Mulhall tornado on 3 May 1999. *J. Atmos. Sci.*, **62**: 2373-2393.

Lewellen, D.C., W.S. Lewellen and J. Xia, 2000. The influence of a local swirl ratio on tornado intensification near the surface. *J. Atmos Sci.*, **57**: 527-544.

Lewellen, D. C., B. Gong, and W. S. Lewellen, 2008. Effects of fine-scale debris on near-surface tornado dynamics. *J. Atmos. Sci.*, **65**: 3247-3262.

Lighthill, M.J., 1952. On sound generated aerodynamically, I. General Theory. *Proc. Roy. Soc. London*, **211 A**: 564-587.

Louis, J.-F., 1979. A parametric model of vertical eddy fluxes in the atmosphere. *Bound.-Lay. Meteor.*, **17**: 187-202.

McWilliams, J.C., L.P. Graves, and M.T. Montgomery, 2003. A formal theory for vortex Rossby waves and vortex evolution. *Geophys. & Astrophys. Fluid Dyn.*, **97**: 275-309.

Medvigy, D, P. R. Moorcroft, R. Avissar and R. L. Walko, 2005. Mass conservation and atmospheric dynamics in the Regional Atmospheric System (RAMS). *Environmental Fluid mechanics*, **5**: 109-34.

Meecham, W.C. and G.W. Ford, 1958. Acoustic radiation from isotropic turbulence. *J. Acoust. Soc. Amer.*, **30**: 318-322.

Meyers, M.P., R.L. Walko, J.Y. Harrington and W.R. Cotton, 1997. New RAMS cloud microphysics parameterization. Part II: The two-moment scheme. *Atmos. Res.*, **45**: 3-39.

Montgomery, M.T., and R.J. Kallenbach, 1997. A theory of vortex Rossby-waves and its application to spiral bands and intensity changes in hurricanes. *Quart. J. Roy. Meteorol. Soc.*, **123**: 435-465.

Nicholls, M.E., and R.A. Pielke Sr., 2000. Thermally induced compression waves and gravity waves generated by convective storms. *J. Atmos. Sci.*, **57**: 3251-3271.

Nicholls, M.E., R.A. Pielke Sr., and A. Bedard, 2004. Preliminary numerical simulations of infrasound generation processes by severe weather using a fully compressible numerical model. *22nd Conference on Severe Local Storms*, Amer. Meteo. Soc., paper 8A.3.

Nolan, D.S., and B.F. Farrell, 1999. Generalized stability analysis of asymmetric disturbances in one- and two-celled vortices maintained by radial inflow. *J. Atmos. Sci.*, **56**: 1282-1307.

Powell, A., 1964. Theory of vortex sound. *J. Acoust. Soc. Amer.*, **36**: 177-195.

Proudman, I., 1952. The generation of noise by isotropic turbulence, *Proc. R. Soc. London*, Ser. A **214**: 119-132.

Rotunno, R., 1977. Numerical simulation of a laboratory vortex. *J. Atmos. Sci.*, **34**: 1942-1956.

Saffman, P.G., 1992. *Vortex Dynamics*, Cambridge University Press, Cambridge, 311 pp.

Saleeby, S.M., and W.R. Cotton, 2004. A large-droplet mode and prognostic number concentration of cloud droplets in the Colorado State University Regional Atmospheric Modeling System (RAMS). Part I: Module descriptions and supercell test simulations. *J. Appl. Meteor.*, **43**: 182-195.

Schecter, D.A., 1999. On the dynamics of inviscid relaxation in 2D fluids and nonneutral plasmas. Ph.D. dissertation, U.C. San Diego, 160 pp.

Schecter, D.A., D.H.E. Dubin, A.C. Cass, C.F. Driscoll, I.M. Lansky and T.M. O'Neil, 2000. Inviscid damping of asymmetries on a two-dimensional vortex.*Phys. of Fluids*, **12**: 2397-2412.

Schecter, D.A., and M. T. Montgomery, 2003. On the symmetrization rate of an intense geophysical vortex. *Dyn. Atmos. Oceans*, **37**: 55-88.

Schecter, D.A., and M.T. Montgomery, 2004. Damping and pumping of a vortex Rossby wave in a monotonic cyclone: critical layer stirring versus inertia-buoyancy wave emission. *Phys. Fluids* **16**: 1334-1348.

Schecter, D.A., M.E. Nicholls, J. Persing, A.J. Bedard Jr. and R.A. Pielke Sr., 2008. Infrasound emitted by tornado-like vortices: basic theory and a numerical comparison to the acoustic radiation of a single-cell thunderstorm. *J. Atmos. Sci.*, **65**: 685-713.

Schecter, D.A. and M.E. Nicholls, 2010. Generation of infrasound by evaporating hydrometeors in a cloud model. *J. App. Meteor. Clim.*, **49**: 664-675.

Schecter, D.A., 2011. A method for diagnosing the sources of infrasound in convective storm simulations. *J. App. Meteor. Clim.*, **50**: 2526-2542.

Schecter, D.A., 2012. A brief critique of a theory used to interpret the infrasound of tornadic thunderstorms. *Mon. Wea. Rev.*, **140**, 2080-2089.

Sinclair, P.C., 1973. The lower structure of dust devils. *J. Atmos. Sci.*, **30**: 1599-1619.

Stein, R.F., 1967. Generation of acoustic and gravity waves by turbulence in an isothermal stratified atmosphere. *Solar Phys.*, **2**: 385-432.

Szoke, E. J., A. J. Bedard, Jr., E. Thaler and R. Glancy, 2004. A comparison of ISNet data with radar data for tornadic and potentially tornadic storms in Northeast Colorado. *22nd Conference on Severe Local Storms*, Amer. Meteo. Soc., paper 1.2.

Tanamachi, R.L., H.B. Bluestein, W.-C. Lee, M. Bell and A. Pazmany, 2007. Ground-based velocity track display (GBVTD) analysis of W-band Doppler radar data in a tornado near Stockton, Kansas, on 15 May 1999. *Mon. Wea. Rev.*, **135**: 783-800.

Tratt, D.M., M.H. Hecht, D.C. Catling, E.C. Samulon, P.H. Smith, 2003. In situ measurement of dust devil dynamics: Toward a strategy for Mars. *J. Geophys. Res.*, **108**: 5116, 7 pp.

Wakimoto, R.M., and J.W. Wilson, 1989. Non-supercell tornadoes. *Mon. Wea. Rev.*, **117**: 1113-1140.

Walko, R.L., W. R. Cotton, M. P. Meyers and J. Y. Harrington, 1995. New RAMS cloud microphysics parameterization. Part 1: The single-moment scheme. *Atmos. Res.*, **38**: 29-62.

Walko, R.L., W.R. Cotton, G. Feingold and B. Stevens, 2000. Efficient computation of vapor and heat diffusion between hydrometeors in a numerical model. *Atmos. Res.*, **53**: 171-183.

Wood, V.T., and L.W. White, 2008. A skirted Rankine combined vortex model. *24th Conference on Severe Local Storms*, Amer. Meteo. Soc., paper P3.4.